scientific reports

Check for updates

OPEN

# Bone marrow mesenchymal stem cells-derived exosomes protect against β-cell destruction models and kidney injury by suppressing ferroptosis

Jiahui Zhang[1,2], Linbo Wang[1,2], Dongwei Liu[1,2], Zhangsuo Liu[1,2]✉, Zhihong Liu[3]✉ & Sijie Zhou[1,2]✉

**Bone marrow mesenchymal stem cell-derived exosomes (BMSC-EXOs) exhibit therapeutic potential in type 1 diabetes mellitus (T1D). In a streptozotocin (STZ)-induced T1D mouse model, BMSC-EXOs reduced hyperglycemia, prevented weight loss, and alleviated early-stage diabetic kidney injury. These protective effects were associated with preserving pancreatic islet structure, restoring β-cell insulin production, and reducing oxidative stress. Mechanistically, BMSC-EXOs inhibited ferroptosis by up-regulating Glutathione peroxidase 4 (GPX4) expression, decreasing lipid peroxidation, and preventing β-cell and kidney damage. These findings indicate that BMSC-EXOs protect against STZ-induced β-cell destruction models and T1D-related complications by inhibiting ferroptosis, presenting a potential therapeutic approach for diabetes management.**

**Keywords** Type 1 diabetes mellitus (T1D), Bone marrow mesenchymal stem cell-derived exosomes (BMSC-EXOs), Ferroptosis

**Abbreviations**

| | |
|---|---|
| ANOVA | Analysis of variance |
| BMSC-EXO | Bone marrow mesenchymal stem cell-derived exosomes |
| BSA | Bovine serum albumin |
| DAPI | 4′,6-Diamidino-2-phenylindole |
| EGR1 | Early growth response protein 1 |
| ELISA | Enzyme-linked immunosorbent assay |
| GPX4 | Glutathione peroxidase 4 |
| IACUC | Institutional Animal Care and Use Committee |
| KIM1 | Kidney injury molecule 1 |
| MDA | Malondialdehyde |
| MPC5 | Mouse podocyte cell line mouse podocyte clone 5 |
| NGAL | Neutrophil gelatinase-associated lipocalin |
| NTA | Nanoparticle tracking analysis |
| RIPA | Radioimmunoprecipitation assay |
| SDS-PAGE | Sodium dodecyl sulfate polyacrylamide gel electrophoresis |
| STZ | Streptozotocin |
| SYNPO | Synaptopodin |
| TEM | Transmission electron microscopy |
| T1D | Type 1 diabetes mellitus |

[1]Traditional Chinese Medicine Integrated Department of Nephrology, The First Affiliated Hospital of Zhengzhou University, Zhengzhou, China. [2]Research Institute of Nephrology, Zhengzhou University, Zhengzhou, China. [3]National Clinical Research Center of Kidney Diseases, Jinling Hospital, Nanjing University School of Medicine, Nanjing, China. ✉email: zhangsuoliu@zzu.edu.cn; liuzhihong@nju.edu.cn; fcczhousj@zzu.edu.cn

Diabetes mellitus is a significant global health challenge and a leading cause of morbidity and mortality, imposing substantial medical and socioeconomic burdens worldwide. It is classified into Types 1 and 2 diabetes (T1D, T2D)[1]. Type 1 diabetes mellitus (T1D) is an autoimmune disease characterized by T-cell-mediated destruction of pancreatic islet β-cells, resulting in absolute insulin deficiency[2]. Consequently, patients with T1D require lifelong exogenous insulin therapy, which is associated with numerous complications and limitations[3,4]. Diabetic nephropathy is a leading cause of end-stage renal disease worldwide and a major contributor to mortality among patients with diabetes[5,6]. This underscores the urgent need for novel therapeutic strategies to protect or repair β-cell function, potentially enabling endogenous insulin production and improving long-term disease management.

Mesenchymal stem cells (MSCs) are multipotent cells capable of differentiating into various mature mesenchymal tissues. Due to their low immunogenicity, MSCs are considered ideal candidates for cell-based transplantation[7,8]. However, their therapeutic application is limited by challenges such as poor organ retention, the risk of microthrombosis, host immune responses, and tumorigenicity potential[9,10]. The therapeutic effects of MSCs are primarily mediated through paracrine signaling[11]. Exosomes are extracellular vesicles, 30–150 nm in diameter, enclosed by a lipid bilayer and secreted into the extracellular environment[12]. Recent studies have highlighted that MSC-derived exosomes (MSC-EXOs) can be as effective as MSCs in treating diabetes mellitus and its complications[10,13]. Unlike MSCs, which are 30–60 μm in diameter, nano-sized exosomes can more effectively reach target tissues after systemic administration, avoiding entrapment in the pulmonary microvasculature and thereby reducing the risk of pulmonary embolism caused by cell aggregation[14]. Bone marrow MSC-EXOs (BMSC-EXOs) are considered the optimal seed cells for therapeutic applications due to the ease of isolating and culturing BMSC in vitro and their high proliferation rate[15]. BMSC-EXOs carry a wide range of bioactive molecules, such as proteins, lipids, and microRNAs, which modulate critical cellular processes, including oxidative stress, apoptosis, and inflammation[16,17]. In streptozotocin (STZ)-induced T1D rat models, BMSC-EXOs have been shown to promote pancreatic islet regeneration, increase the number and size of Langerhans islets, and reduce local inflammation and fibrotic remodeling. Collectively, these effects help preserve endogenous insulin production and mitigate autoimmune-mediated β-cell destruction, thereby slowing T1D progression[18]. Further studies are needed to elucidate the underlying mechanisms.

Ferroptosis is an iron-dependent form of regulated cell death. Emerging evidence suggests that ferroptosis plays a critical role in pancreatic β-cell dysfunction and diabetic kidney injury[19–21]. Its underlying mechanisms include dysregulation of iron metabolism, lipid peroxidation, and suppression of the antioxidant defense system[22,23]. Pancreatic β-cells inherently exhibit weak antioxidant capacity and are particularly vulnerable to oxidative stress[24]. In type 1 diabetes (T1D), the inflammatory microenvironment and elevated reactive oxygen species (ROS) levels disrupt intracellular redox homeostasis, thereby initiating ferroptotic cell death[25]. Additionally, iron metabolism disorders, commonly observed under diabetic conditions, can intensify lipid peroxidation via the Fenton reaction, further amplifying cellular injury[23,26]. The chronic hyperglycemic state of T1D not only promotes iron accumulation in pancreatic tissue but also exacerbates ferroptosis in other organs such as the kidney and heart, thereby contributing to the progression of diabetic complications. For example, in diabetic cardiomyopathy, iron and ROS released from ferroptotic cardiomyocytes create a pro-fibrotic microenvironment that promotes fibroblast activation and sustains tissue fibrosis[27,28]. Similarly, in mouse models of diabetic nephropathy, excessive iron deposition and reduced antioxidant capacity have been observed in renal tubules. High-glucose stimulation of HK-2 cells also leads to elevated MDA and iron levels, triggering ferroptosis and aggravating renal injury[29]. Therefore, targeting ferroptosis-related pathways, such as inhibiting lipid peroxidation, modulating iron metabolism, or activating antioxidant defenses, may offer novel therapeutic strategies for the prevention and treatment of T1D and its complications.

Given the therapeutic potential of BMSC-EXOs and the established role of ferroptosis in diabetes-related complications, this study aimed to investigate whether BMSC-EXOs therapy could attenuate T1D-induced β-cell injury and diabetic kidney damage by inhibiting ferroptosis. Using an STZ-induced murine model of T1D, we evaluated the protective effects of BMSC-EXOs on pancreatic islets and kidney tissues while elucidating the molecular mechanisms underlying ferroptosis inhibition. Our findings provide novel insights into exosome-based therapeutic strategies for mitigating T1D-associated complications.

## Materials and methods

### Animal experiment design

All animal experiments were performed in accordance with relevant institutional and national guidelines for animal use. The experimental protocols were approved by the Institutional Animal Care and Use Committee (IACUC) of Zhengzhou University (Ethics Approval NO. ZZU-LAC20230804[20]). This study also complies with the ARRIVE guidelines (https://arriveguidelines.org). C57BL/6J mice were obtained from GemPharmatech Company (Nanjing, Jiangsu, China). Chow (Lab diet 5001, LabDiets, St. Louis, MO, USA) and water were provided ad libitum.

A murine model of streptozotocin (STZ)-induced diabetes was established in 8-week-old male C57BL/6 mice by intraperitoneal (I.P.) injection of STZ (55 mg/kg/day), dissolved in 50 mM sodium citrate buffer (pH 4.5), administered once daily for five consecutive days. Control group mice received injections of sodium citrate buffer without STZ. Two weeks after the final injection, diabetic mice were randomly divided into two treatment groups (n = 5 per group): (1) STZ + phosphate-buffered saline (PBS) group, which received tail vein injections of PBS every 2 days for 2 weeks; and (2) STZ + exosome (STZ + EXO) group, which received tail vein injections of BMSC-EXOs (100 μg in PBS) on the same schedule. Body weight and fasting blood glucose levels were monitored biweekly. After 2 weeks of exosome treatment, all mice were euthanized by $CO_2$ inhalation, and tissue, blood, and urine samples were collected for biochemical, histological, and molecular analyses.

In a separate experiment, mice injected with STZ were randomly assigned into the following groups (n = 5 mice/group): (1) EXO + AAV-GPX4 group: mice received BMSC-EXOs and adeno-associated virus (AAV) carrying GPX4 gene (AAV-GPX4) through tail vein; (2) EXO + AAV-NC (negative control) group: mice received BMSC-EXOs and AAV carrying a scrambled sequence of the GPX4 gene (AAV-NC); (3) EXO + shGPX4 group: mice received BMSC-EXOs and AAV carrying a short hairpin RNA (shRNA) targeting GPX4 to knock down its expression; (4) EXO + shNC group: mice received BMSC-EXOs and AAV carrying a non-targeting negative control shRNA sequence. After 2 weeks of exosome treatment, all mice were euthanized by $CO_2$ inhalation, and samples were collected for biochemical, histological, and molecular analyses. AAV purchases from Company Hanbio Biotechnology, Inc. (Shanghai, China).

## Cell culture

Bone marrow mesenchymal stem cells (BMSCs) were isolated from the femurs and tibias of 4–6-week-old mice. Cells were seeded in a complete BMSCs culture medium (CM-M131, Wuhan Pricella Biotechnology Co., Ltd., China) at an initial density of $5 \times 10^3$ cells/cm$^2$ for routine passaging and differentiation. Cultures were maintained at 37 °C in a humidified incubator with 5% $CO_2$ and 5% $O_2$. After 24 h, the culture medium was replaced and then refreshed every 12 h to remove non-adherent cells. After 72 h, the medium was subsequently changed every 2–3 days. When cultures reached 60–80% confluency, cells were passaged at a 1:3 ratio. BMSCs in passages 3–5 were used in subsequent experiments. Cell morphology was monitored and documented using light microscopy.

The conditionally immortalized mouse podocyte cell line, mouse podocyte clone 5 (MPC5), was obtained from the Cell Bank of the Chinese Academy of Sciences (Shanghai, China). MPC5 cells were seeded at $5 \times 10^4$ cells/cm$^2$ in collagen I-coated culture plates and maintained in RPMI-1640 medium (Life Technologies, Grand Island, NY, USA) supplemented with 10% fetal bovine serum (FBS; Life Technologies) and antibiotics (100 U/mL penicillin and 100 µg/mL streptomycin) (10378016, Thermo Fisher Scientific, USA). For proliferation, MPC5 cells were cultured at 33 °C in the presence of 10 U/mL interferon-γ (IFN-γ). To induce differentiation, cells were cultured at 37 °C without IFN-γ for 10–14 days prior to experiments. At 50–60% confluency, MPC5 cells were treated under the following conditions for 48 h: (1) HM + PBS group: Normal glucose (5.6 mM) + high mannitol (24.4 mM) + PBS; (2) high glucose (HG) + PBS group: High glucose (30 mM) + PBS; and (3) HG + EXO group: High glucose (30 mM) + BMSC-EXOs (100 µg/mL).

## Flow cytometry analysis of BMSCs surface markers

BMSCs at passage 3 were harvested using 0.25% trypsin–EDTA (Sigma-Aldrich) and washed with PBS. A total of $5 \times 10^6$ cells were resuspended in PBS and incubated with antibodies targeting the following surface markers: CD34$^-$ (Cat# 119328, BioLegend, USA), HLA-DR$^-$ (Cat# 756955, BioLegend), CD45$^-$ (Cat# 103112, BioLegend), CD90$^+$ (Cat# 105305, BioLegend), CD73$^+$ (Cat# 127205, BioLegend), and CD105$^+$ (Cat# 120407, BioLegend). Antibodies were added to 100 µL cell suspensions and incubated at 4 °C in the dark for 30 min. After incubation, the cells were washed and analyzed within 1 h using a FACS Canto I flow cytometer (BD Biosciences, USA). Data were processed and analyzed using FlowJo software (version 10). Unstained cells served as negative controls to account for autofluorescence.

## BMSCs differentiation assays

Osteogenic differentiation of mouse bone marrow mesenchymal stem cells (BMSCs) was performed using a commercial osteogenic differentiation kit (MUXMX-90021, Oricell Therapeutics Co., Ltd., Guangzhou, China) according to the manufacturer's instructions. Briefly, when BMSCs reached approximately 70% confluence, the culture medium was replaced with osteogenic differentiation medium, which was refreshed every 3 days. After 2–4 weeks of induction, osteogenic differentiation was confirmed by Alizarin Red S staining to detect calcium deposits.

Adipogenic differentiation of BMSCs was performed using a commercial adipogenic differentiation kit (MUXMX-90021, Oricell Therapeutics Co., Ltd., Guangzhou, China) according to the manufacturer's instructions. Briefly, when the cells reached 100% confluence, the culture medium was replaced with Adipogenic Differentiation Medium A for 3 days, followed by Adipogenic Differentiation Medium B for 1 day. Thereafter, the cells were alternately cultured with Medium A (3 days) and Medium B (1 day) until adequate and appropriately sized lipid droplets appeared. Adipogenic differentiation was confirmed by Oil Red O staining of intracellular lipid droplets.

## Exosome isolation

The exosomes were isolated using a sequential centrifugation protocol[30]. First, cell debris was removed by centrifugation at 2000×*g* for 10 min, followed by an additional centrifugation at 10,000×*g* for 30 min at 4 °C. The resulting supernatant was filtered through a 0.22-µm filter to remove residual contaminants. Exosomes were then pelleted by ultracentrifugation at 200,000×*g* for 120 min at 4 °C using an Optima XPN-100 Ultracentrifuge (Beckman Coulter, USA). The pellet was resuspended in PBS, and the protein concentration was measured using a BCA protein assay kit (Solarbio). The concentration and size of the exosomes were analyzed using a Flow Nano Analyzer (N30E, NanoFCM Inc., China).

## Blood glucose level measurements

The mice underwent a 6 h fasting period before blood collection. Blood samples were collected using the submandibular bleeding method. Blood glucose levels were measured immediately using a glucometer and OneTouch Ultra Test Strips (Life Scan Europe, Inverness, UK) to ensure accurate and consistent readings.

### Isolation of mouse islets

Pancreatic islets were isolated from euthanized mice using collagenase digestion followed by density gradient centrifugation[31]. Collagenase solution (1.7 mg/mL, Sigma-Aldrich) was injected into the pancreas via the common bile duct, followed by digestion at 37 °C for 20 min. The islets were then separated and manually selected under a microscope.

### Isolation of glomeruli

Glomeruli were isolated by perfusing 5 mL of PBS containing $8 \times 10^7$ Dynabeads M-450 (Dynal Biotech ASA) into the kidneys via the abdominal aorta[32]. The kidneys were minced into 1-$mm^3$ fragments and digested with 1 mg/mL collagenase (Sigma-Aldrich) at 37 °C for 30 min. The digested tissue was filtered through a 100 µm cell strainer, and glomeruli containing Dynabeads were collected using a magnetic particle concentrator.

### Urine analyses

Urine samples (10 µL) were analyzed via SDS-PAGE, followed by Coomassie Brilliant Blue staining. To serve as a reference, BSA was loaded at three different concentrations: 1 µg, 3 µg, and 6 µg. Albumin and creatinine concentrations were quantified using a mouse albumin ELISA quantitation kit (Bethyl Laboratories Inc.) and a creatinine assay kit (BioAssay Systems).

### Immunohistochemistry analysis

Pancreatic and kidney tissues were fixed in formalin, embedded in paraffin, and sectioned into 3–5 µm slices for histological analysis. Hematoxylin and eosin (H&E) staining was performed to evaluate tissue morphology. ImageJ software (NIH, USA) was used to quantify the islet-to-pancreas area (%), islet density, and average islet-positive area in the pancreas[33]. Immunohistochemical staining of pancreatic tissue was performed using antibodies against insulin (1:10,000; c27c9, Cell Signaling Technology, Danvers, MA, USA) and GPX4 (1:1000; Ab125066, Abcam, Cambridge, MA, USA). For kidney tissue, immunostaining was conducted using antibodies against GPX4 (1:1000; Ab125066, Abcam) and KIM1 (1:400; NBPI-76701, Novus Biologicals, Centennial, CO, USA). After primary antibody incubation, horseradish peroxidase (HRP)-conjugated secondary antibodies were applied and incubated for 60 min at room temperature. Diaminobenzidine (DAB) was used as the chromogen to visualize positive staining. Protein expression levels were quantified by calculating the average gray value from five randomly selected fields per sample at 400× magnification. Positive staining and total tissue areas were measured using ImageJ software. Signals appearing as light yellow, brown-yellow, or dark brown were considered positive. The percentage of positive expression was calculated using the formula[34]:

$$Percentage = \frac{Area\ of\ positive\ staining}{Total\ tissue\ area}$$

### Immunofluorescence staining

Kidney tissues were embedded in OCT, snap-frozen, and sectioned at a thickness of 5 µm. The sections were fixed with 4% paraformaldehyde, blocked with 5% BSA, and incubated overnight at 4 °C with primary antibodies against SYNPO (1:200, sc-515842, Sigma-Aldrich) and Neutrophil gelatinase-associated lipocalin (NGAL) (1:200, sc-515876, Santa Cruz biotechnology). The cultured cells were similarly fixed with 4% paraformaldehyde, permeabilized with 0.2% Triton X-100, and blocked with 5% BSA. These cells were then incubated overnight at 4 °C with primary antibodies targeting SYNPO (1:200, sc-515842, Sigma-Aldrich) or EGR1 (1:200, H00001958-M03, ABNOVA). Following washing steps, sections were treated with fluorophore-conjugated secondary antibodies (1:200, Alexa Fluor 488 or 594) for 1 h at room temperature. Nuclei were stained with 4′,6-diamidino-2-phenylindole (DAPI, Vector Laboratories, Burlingame, CA, USA), and the sections were mounted using an anti-fade medium. Images were captured using a fluorescence microscope, and fluorescence intensity was analyzed to assess podocyte integrity and tubular injury.

MPC5 were seeded on sterile coverslips. After fixation with 4% paraformaldehyde for 15 min and PBS washing, TUNEL staining was performed according to the TUNEL Assay Kit (C10617, Thermo Fisher Scientific). Subsequently, cells were incubated with propidium iodide (PI, 50 µg/mL) at room temperature in the dark for 10 min. After staining, coverslips were mounted, and images were captured using a fluorescence microscope. Quantification was performed by counting positive cells in five randomly selected fields per sample. All experiments were independently repeated at least three times.

### Western immunoblot analysis

Exosome samples, pancreatic islets, renal glomeruli, kidney tissues, and cultured podocytes were homogenized in RIPA buffer supplemented with protease inhibitors[35] to extract total protein. For each sample, 20–50 µg of total protein was loaded per lane on SDS-PAGE gels. Western blotting was performed using primary antibodies against the following proteins: Tsg101 (1:1000, EXOAB-TSG101-1, System Biosciences), CD9 (1:1000, EXOAB-CD9A-1, System Biosciences), CD63 (1:1000, EXOAB-CD63A-1, System Biosciences), SYNPO (1:1000, sc-515842, Santa Cruz Biotechnology), GPX4 (1:1000, Ab125066, Abcam), EGR1 (1:1000, H00001958-M03, ABNOVA), NGAL (1:1000, sc-515876, Santa Cruz Biotechnology), cleaved caspase-3 (1:1000, 9661S, Cell Signaling Technology), insulin (1:1000, L-8138, Cell Signaling Technology), and KIM1 (1:1000, NBPI-76701, Novus Biologicals). β-actin (1:5000, ZB15001-HRP, Servicebio) and GAPDH (1:4000, sc-32233, Santa Cruz Biotechnology) served as loading controls. Protein expression levels were quantified by densitometry to evaluate the effects of exosome therapy on pancreatic and kidney injury.

### Cell viability assay
Podocyte viability was assessed using the Cell Counting Kit-8 (CCK-8; CK04, Dojindo, Kumamoto, Japan) following the manufacturer's instructions. A total of $1 \times 10^3$ cells were seeded into each well of a 96-well plate. After cell attachment, PBS or exosomes were added according to the experimental design. Following 48 h of incubation, the cells were further incubated at 37 °C for 2 h with CCK-8 reagent. Absorbance at 450 nm was measured using a microplate reader (Molecular Devices, Shanghai, China).

### Determination of iron content
Ferrous iron levels in kidney cortex tissues and MPC5 cells were measured using the Iron Assay Kit (MAK025, Sigma-Aldrich, St. Louis, MO, USA) according to the manufacturer's instructions. Kidney cortex tissues (10 mg) were homogenized, and MPC5 cells ($5 \times 10^6$) were collected and lysed using an ultrasonic cell disrupter (Scientz, China). The homogenates were centrifuged, and the supernatants were collected for analysis. Absorbance was measured at 593 nm using a microplate reader.

### Determination of malondialdehyde (MDA) levels
MDA levels in pancreatic islet and kidney cortex tissues were assessed using the Lipid Peroxidation MDA Assay Kit (S0131, Beyotime, Shanghai, China) following the manufacturer's instructions. Tissue samples were homogenized and centrifuged to collect supernatants. Absorbance was measured at 532 nm using a microplate reader. MDA concentrations were normalized to the total protein content in the tissue homogenates.

### Transmission electron microscopy (TEM)
Mouse kidney tissues and BMSC-EXOs were fixed in glutaraldehyde and post-fixed in 1% osmium tetroxide. Samples were dehydrated through a graded acetone series and embedded in 812 epoxy resin. Polymerization was conducted at 60 °C. Ultrathin sections (~60 nm) were prepared using an ultramicrotome and stained with uranyl acetate and lead citrate. Images were acquired using a transmission electron microscope (Hitachi, Tokyo, Japan).

### In vivo fluorescence imaging of DiR-labeled BMSC-EXOs
To assess the biodistribution of BMSC-derived exosomes in vivo, exosomes were labeled with the near-infrared fluorescent dye DiR (excitation/emission: 754/778 nm; D12731, Thermo Fisher Scientific) according to the manufacturer's instructions. Briefly, 200 μg of exosomes were incubated with 4 μg of DiR dye in PBS at 37 °C for 30 min in the dark. Free dye was removed via ultracentrifugation at 100,000×*g* for 30 min at 4 °C, and the labeled exosomes were resuspended in sterile PBS.

Three weeks after STZ induction, mice received tail vein injections of 100 μg DiR-labeled BMSC-EXOs or PBS. A second injection (100 μg) was administered 6 h later. After 24 h, mice were anesthetized (isoflurane, 2% maintenance in $O_2$:$N_2O$; 1:1) and subjected to in vivo fluorescence imaging using a small animal imaging system (IVIS Lumina III, PerkinElmer, USA). Fluorescence intensity was analyzed to assess exosome distribution. Mice were then euthanized, and major organs (e.g., kidney, pancreas) were harvested for ex vivo fluorescence imaging to evaluate organ-specific accumulation of exosomes.

### Statistical analysis
The normality of the data was confirmed using the Shapiro–Wilk test and the results are presented as mean ± standard deviation (SD). Statistical comparisons between groups were performed using one-way analysis of variance (ANOVA) followed by Tukey's post-hoc test. A $p$ value of $< 0.05$ was considered statistically significant. Sample sizes were determined based on power analysis to ensure adequate statistical power. In the figures, asterisks denote levels of statistical significance as follows: *: $p < 0.05$, **: $p < 0.01$ and ***: $p < 0.001$.

## Results
### Characterization of BMSC-EXOs for therapeutic potential
The identity and functionality of BMSCs and their derived exosomes were characterized through a series of morphological and molecular analyses. Bright-field microscopy confirmed the typical fibroblast-like morphology of cultured BMSCs (Fig. 1A). The multipotency of BMSCs was demonstrated through differentiation assays, in which cells successfully differentiated into osteogenic and adipogenic lineages, as indicated by calcium deposition stained with Alizarin Red and lipid droplet accumulation stained with Oil Red O (Fig. 1B). The surface markers of BMSCs were analyzed by flow cytometry. The cells exhibited high expression of CD105 (99.9%), CD73 (99.1%), and CD90 (95.1%), while CD34, CD45, and HLA-DR were not expressed (Fig. 1C). These results confirm that the mouse BMSCs display typical mesenchymal stem cell characteristics. TEM revealed a cup-shaped morphology of the isolated exosomes, confirming their characteristic ultrastructure (Fig. 1D). Western blot analysis further validated the identity of the exosomes by detecting the positive expression of exosome markers CD9, CD63, and TSG101 (Fig. 1E). Nanoparticle tracking analysis (NTA) determined the size distribution of exosomes, with a peak diameter of approximately 100 nm, which was consistent with typical exosome dimensions (Fig. 1F). These findings confirm the successful isolation and characterization of BMSC-EXOs, underscoring their potential for therapeutic applications.

### BMSC-EXOs therapy repairs STZ-induced hyperglycemia, weight loss, and pancreatic islet damage
This figure illustrates the experimental design and the reparative effects of BMSC-EXOs on STZ-induced T1D in mice. T1D was induced by administering a low-dose STZ regimen over five consecutive days, followed by BMSC-EXOs administration every other day for 2 weeks, starting from the second week (Fig. 2A). To track the

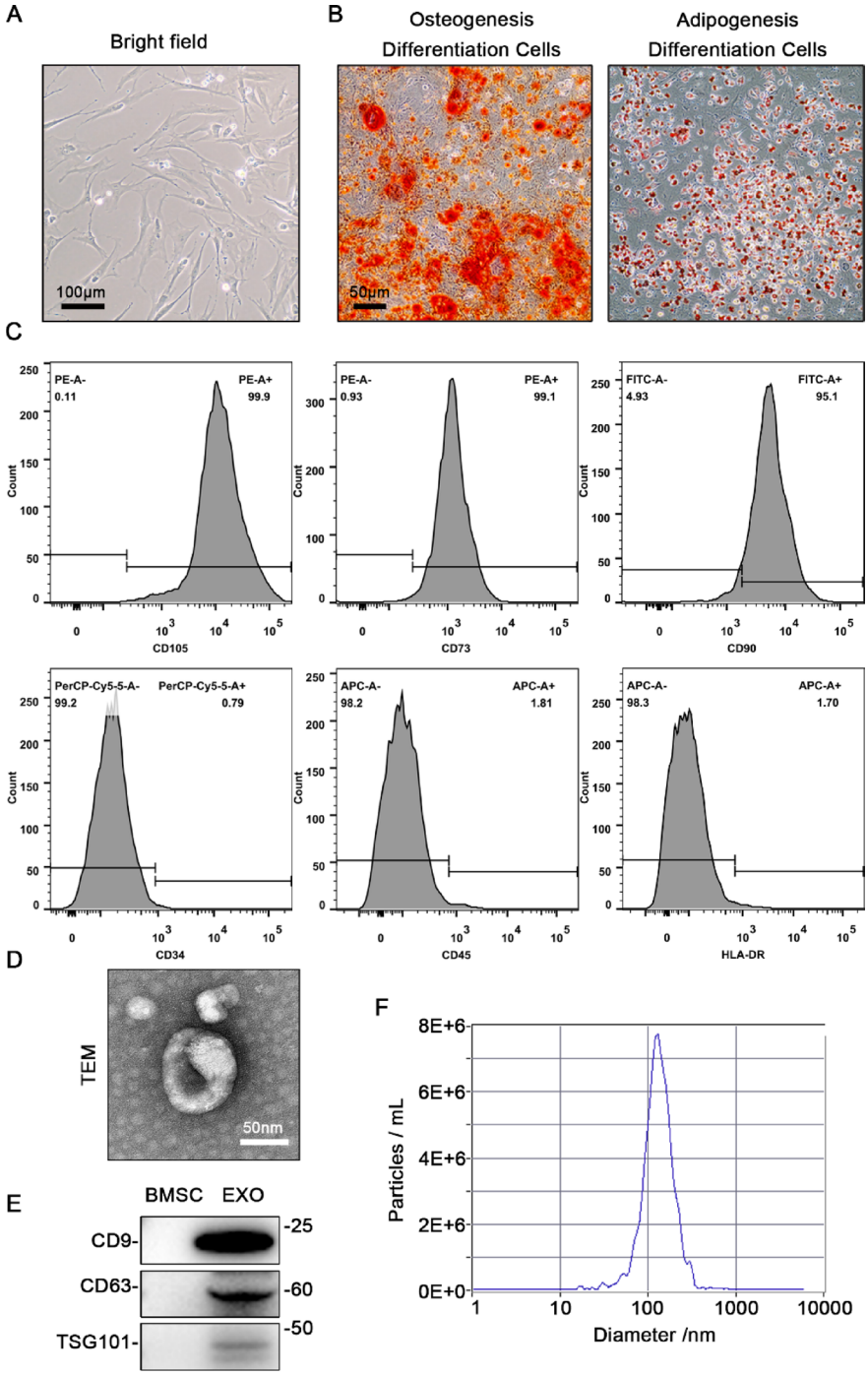


**Fig. 1**. Characterization of BMSC-EXOs for therapeutic potential. (**A**) Morphology of BMSCs cultured in regular medium at passage 3. Scale bar = 100 μm. (**B**) Differentiation potential of BMSCs confirmed by osteogenic (Alizarin Red staining) and adipogenic (Oil Red O staining) differentiation. Scale bar = 50 μm. (**C**) Flow cytometry analysis of BMSCs surface markers. The BMSCs were positive for CD105, CD73, and CD90, and negative for CD34, CD45, and HLA-DR. (**D**) TEM image of BMSCs-derived exosomes showing their typical cup-shaped structure. Scale bar = 50 nm. (**E**) Western blot analysis confirms exosome markers CD9, CD63, and TSG101. (**F**) Nanoparticle tracking analysis (NTA) shows exosome size distribution. *BMSCs* bone marrow mesenchymal stem cells, *TEM* transmission electron microscopy, *NTA* nanoparticle tracking analysis.

biodistribution of BMSC-EXOs, DiR-labeled exosomes were injected. In vivo fluorescence imaging revealed strong signals in the abdominal region in the STZ + EXO group (Fig. 2B). Ex vivo imaging of dissected organs confirmed a substantial accumulation of exosomes in the pancreas and kidneys of the STZ + EXO group (Fig. 2C). STZ injections caused a significant increase in fasting blood glucose levels over time, confirming the onset of hyperglycemia. Treatment with BMSC-EXOs markedly reduced blood glucose levels compared

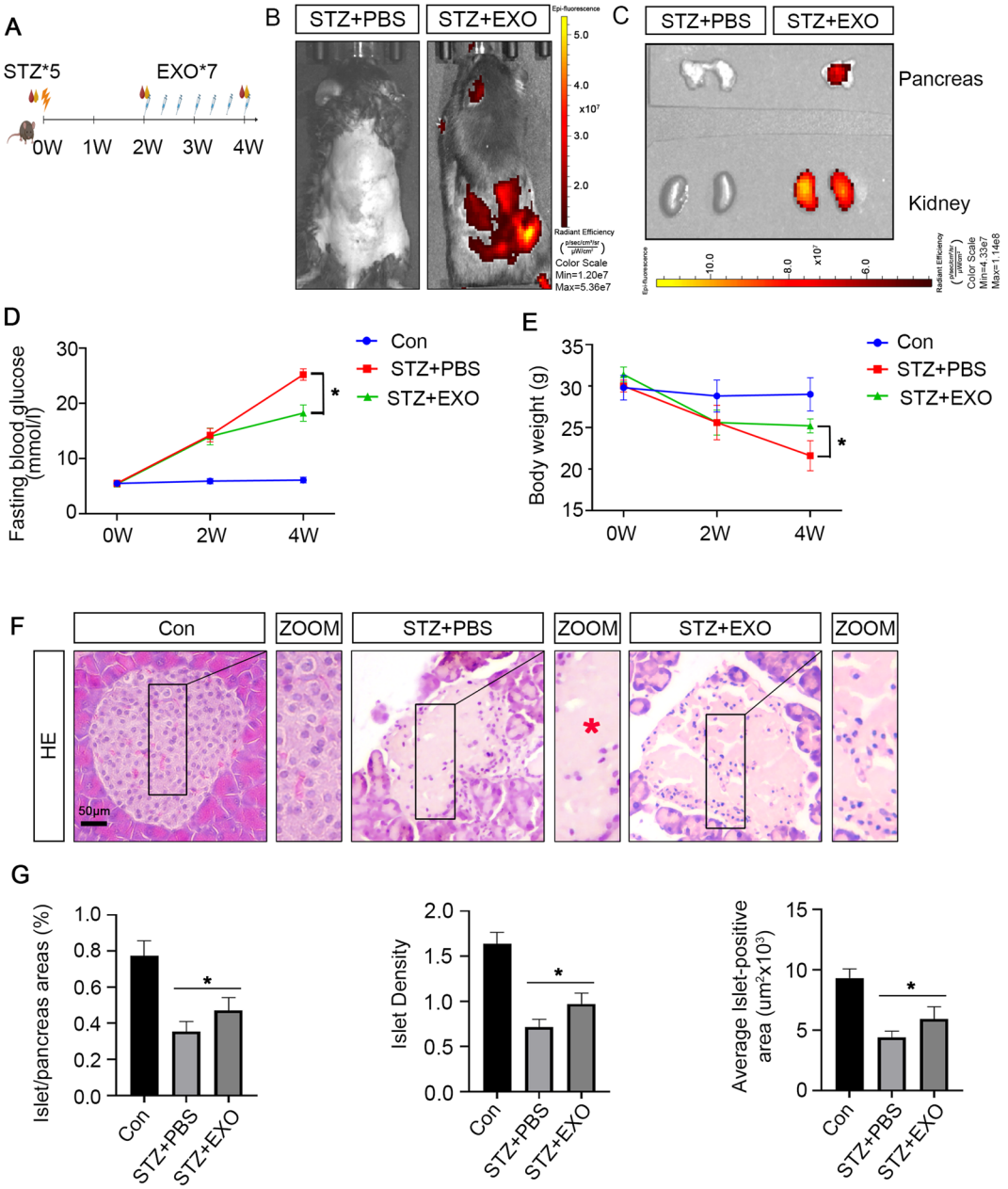


**Fig. 2**. BMSC-EXOs therapy repairs STZ-induced hyperglycemia, weight loss, and pancreatic islet damage. (**A**) Schematic of the experimental timeline showing STZ induction and EXO treatment. (**B**) In vivo fluorescence imaging of DiR-labeled BMSC-EXOs 24 h after tail vein injection. Yellow indicates regions of high fluorescence intensity. (**C**) Ex vivo fluorescence imaging of the pancreas and kidneys, showing organ-specific distribution of BMSC-EXOs. Yellow denotes high fluorescence intensity. (**D**) Fasting blood glucose levels over time in different groups. (**E**) Body weight changes over time in different groups. (**F**) H&E staining of pancreatic islets from control, STZ + PBS, and STZ + EXO groups with zoomed-in views. Pancreatic islet necrosis, characterized by nuclear loss, is indicated by red asterisks. Scale bar = 50 μm. (**G**) Quantification of islet-to-pancreas area ratio, islet density, and average islet-positive area. Each bar represents the mean ± SD of the data derived from five independent experiments (n = 5). *$p < 0.05$. *EXO* exosome, *H&E* hematoxylin–eosin, *PBS* phosphate-buffered saline, *STZ* streptozotocin.

to the untreated STZ group (Fig. 2D). Figure 2E depicts a progressive decline in body weight in STZ-treated mice, which was substantially mitigated by BMSC-EXOs therapy (Fig. 2E). Histological analysis revealed that pancreatic islets in the control group remained intact with well-defined structures. In contrast, treatment with STZ + PBS induced significant islet injury, characterized by diffuse pancreatic islet necrosis with preservation of the exocrine acinar epithelium, ductal structures, and connective tissues. This was accompanied by a reduction in islet size and a decreased number of islets. Treatment with BMSC-EXOs (STZ + EXO) ameliorated these structural abnormalities, preserving islet architecture and integrity (Fig. 2F). Quantitative analysis demonstrated

that BMSC-EXOs therapy counteracted STZ-induced reductions in the islet-to-pancreas area ratio, islet density, and average islet-positive area (Fig. 2G). These findings indicate that BMSC-EXOs exert a protective effect in diabetes by alleviating hyperglycemia, preventing body weight loss, and mitigating pancreatic islet injury. By preserving pancreatic islet morphology, protecting β-cells from STZ-induced damage, and maintaining islet structure and function, BMSC-EXOs show significant therapeutic potential for diabetes management.

## Reparative effects of BMSC-EXOs therapy on ferroptosis and β-cell dysfunction in STZ-induced pancreatic islet injury

STZ treatment significantly reduces insulin expression, indicating significant β-cell dysfunction. BMSC-EXOs therapy effectively improves insulin levels, demonstrating its potential to repair β-cell functions. In the STZ + PBS group, Glutathione peroxidase 4 (GPX4), a key regulator of ferroptosis, was markedly downregulated, indicating increased susceptibility to ferroptosis-induced damage. Treatment with BMSC-EXOs improved GPX4 expression, highlighting its role in mitigating ferroptosis (Fig. 3A–C). Immunohistochemical staining revealed a substantial reduction in insulin and GPX4 expression in the STZ + PBS group, whereas the STZ + EXO group exhibited marked restoration of both markers, indicating preservation of islet structure and function (Fig. 3D–F). Furthermore, STZ-induced ferroptosis was confirmed by elevated iron content and malondialdehyde (MDA) levels, which are markers of oxidative damage and lipid peroxidation, respectively, both of which were significantly reduced following BMSC-EXOs therapy (Fig. 3G,H). Collectively, these findings indicate that BMSC-EXOs treatment repairs β-cell dysfunction suppresses ferroptosis and preserves pancreatic islet function in diabetic conditions.

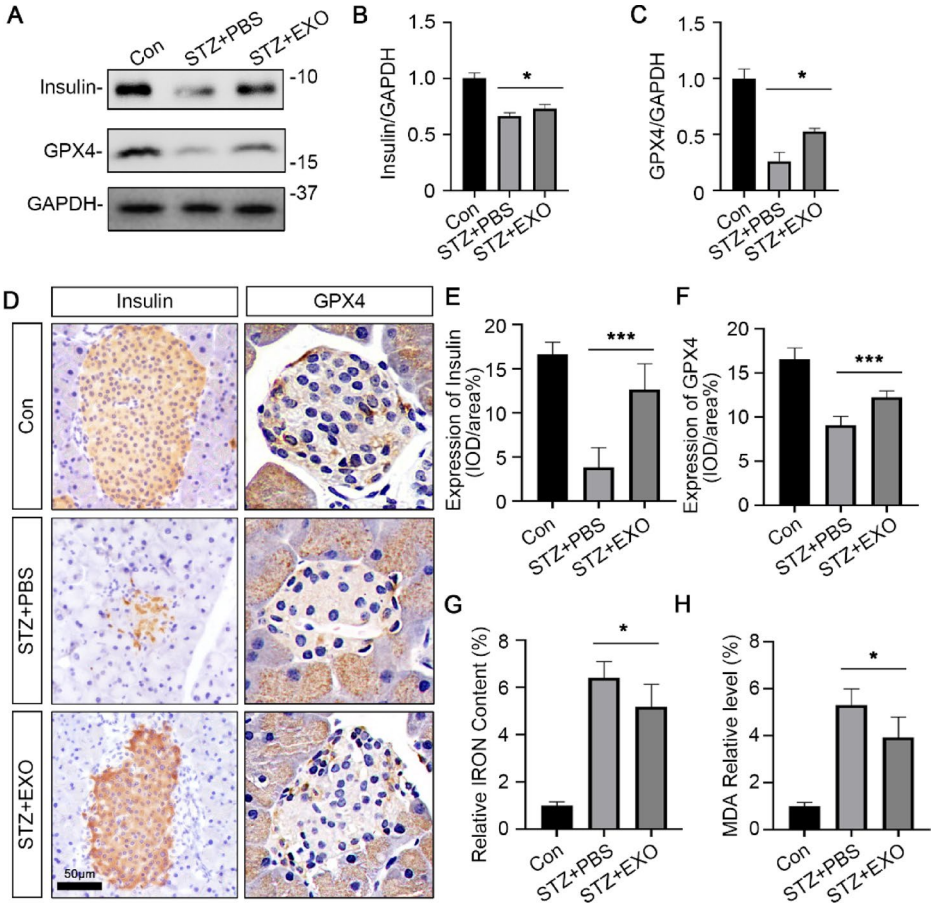


**Fig. 3**. Reparative effects of BMSC-EXOs therapy on ferroptosis and β-cell dysfunction in STZ-Induced pancreatic islet injury. (**A**) Western blot analysis of insulin, GPX4, and GAPDH expression in pancreatic islets. (**B**) Quantification of insulin expression normalized to GAPDH. (**C**) Quantification of GPX4 expression normalized to GAPDH. (**D**) Immunohistochemical staining of pancreatic islets for insulin and GPX4. Scale bar, 50 μm. Semi-quantitative analysis of immunohistochemical staining for insulin (**E**) and GPX4 (**F**) in each group. (**G**) Quantifying relative iron content and (**H**) MDA levels in pancreatic islets. Each bar represents the mean ± SD of the data derived from five independent experiments (n = 5). $^{*}p < 0.05$, $^{***}p < 0.001$. *GAPDH* glyceraldehyde-3-phosphate dehydrogenase, *GPX4* glutathione peroxidase 4, *MDA* malondialdehyde.

## Reparative effects of BMSC-EXOs therapy on STZ-induced diabetic kidney injury

BMSC-EXOs demonstrated significant reparative effects in STZ-induced diabetic kidney injury. STZ treatment led to increased albuminuria, as indicated by elevated urinary protein levels and a higher urinary albumin-to-creatinine ratio (Fig. 4A,B). These pathological changes were significantly attenuated following BMSC-EXOs treatment, indicating improved kidney function. Furthermore, the expression of key kidney injury markers was modulated. Synaptopodin (SYNPO), a marker of podocyte integrity, was significantly reduced in the glomeruli of the STZ + PBS group. NGAL, a marker of tubular injury, and cleaved caspase-3, a marker of apoptosis, were elevated in the kidney of the STZ + PBS group. BMSC-EXOs therapy improved SYNPO expression in the glomeruli and downregulated NGAL and cleaved caspase-3 levels in kidney (Fig. 4C). Quantitative analysis supported these findings, revealing a significant restoration of SYNPO (Fig. 4D) and a concurrent decrease in NGAL and cleaved caspase-3 levels following BMSC-EXOs (Fig. 4E). Immunofluorescence analysis further confirmed these effects, demonstrating the preservation of SYNPO expression in the glomeruli and a reduction in NGAL expression in the renal tubules following BMSC-EXOs (Fig. 4F). These results highlighted the reparative role of BMSC-EXOs in mitigating STZ-induced albuminuria, preserving podocyte integrity, and alleviating tubular injury and apoptosis.

## BMSC-EXOs therapy suppresses ferroptosis and repairs mitochondrial and tubular damage in STZ-induced diabetic kidney injury

BMSC-EXOs effectively inhibited ferroptosis and repaired ferroptosis-induced damage in STZ-induced diabetic kidney injury. Severe mitochondrial damage characterized by cristae loss and swelling was observed in the STZ + PBS group (Fig. 5A). Treatment with BMSC-EXOs repaired mitochondrial integrity, indicating their role in mitigating ferroptosis-related structural damage. Additionally, GPX4 expression was significantly reduced in both the glomeruli and tubules of the STZ + PBS group, whereas BMSC-EXOs therapy repaired GPX4 levels, demonstrating its ability to suppress ferroptosis and protect renal cells. Similarly, Kidney injury molecule 1 (KIM1), a marker of tubular injury, was markedly elevated in the STZ + PBS group but decreased following

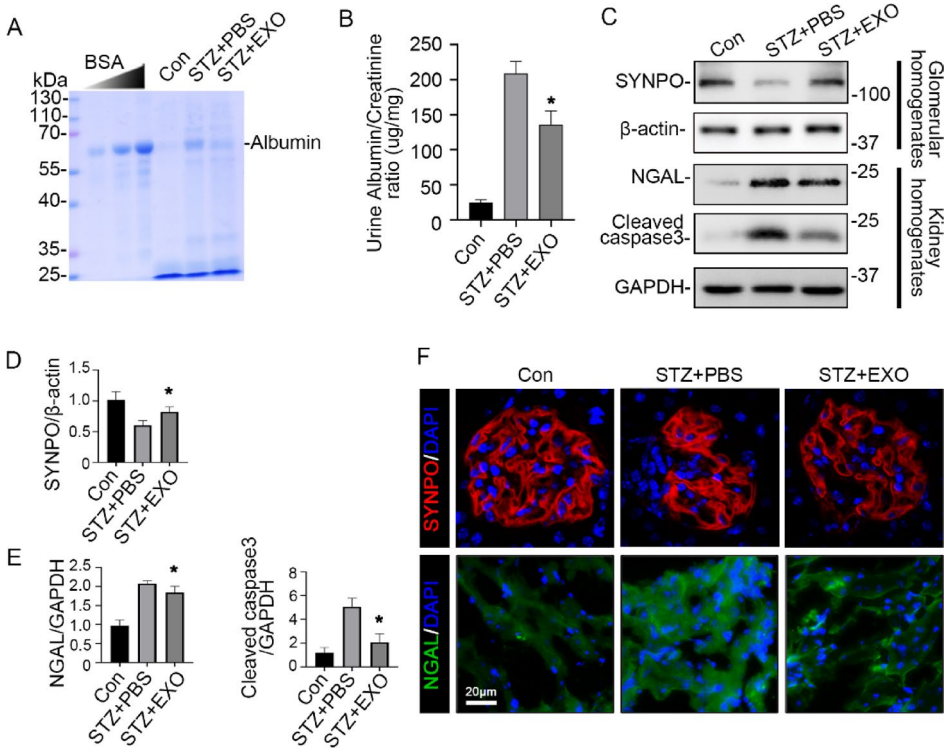


**Fig. 4**. Reparative effects of BMSC-EXOs therapy on STZ-Induced diabetic kidney injury. (**A**) Urine samples (10 μL) were subjected to SDS-PAGE followed by Coomassie brilliant blue staining. BSA (1 μg, 3 μg and 6 μg) served as a standard control. (**B**) Quantification of the urine albumin-to-creatinine ratio in different groups. (**C**) Western blot analysis of SYNPO and β-actin expression in kidney glomerular homogenates. And western blot analysis of NGAL, cleaved caspase-3, and GAPDH expression in kidney homogenates. (**D**) Quantification of SYNPO expression levels in kidney glomerular homogenates. β-actin served as a loading control. (**E**) Quantification of NGAL and cleaved caspase-3 expression levels in kidney homogenates. GAPDH served as a loading control. (**F**) Immunofluorescence staining of renal tissues for SYNPO (red) and NGAL (green), with DAPI (blue) marking nuclei in kidney tissues. Each bar represents the mean ± SD of the data derived from five independent experiments (n = 5). *$p < 0.05$ versus STZ + PBS group. *BSA* Bovine serum albumin, *DAPI* 4′,6-diamidino-2-phenylindole, *NGAL* neutrophil gelatinase-associated lipocalin, *SDS-PAGE* sodium dodecyl sulfate polyacrylamide gel electrophoresis, *STZ* streptozotocin, *SYNPO* synaptopodin.

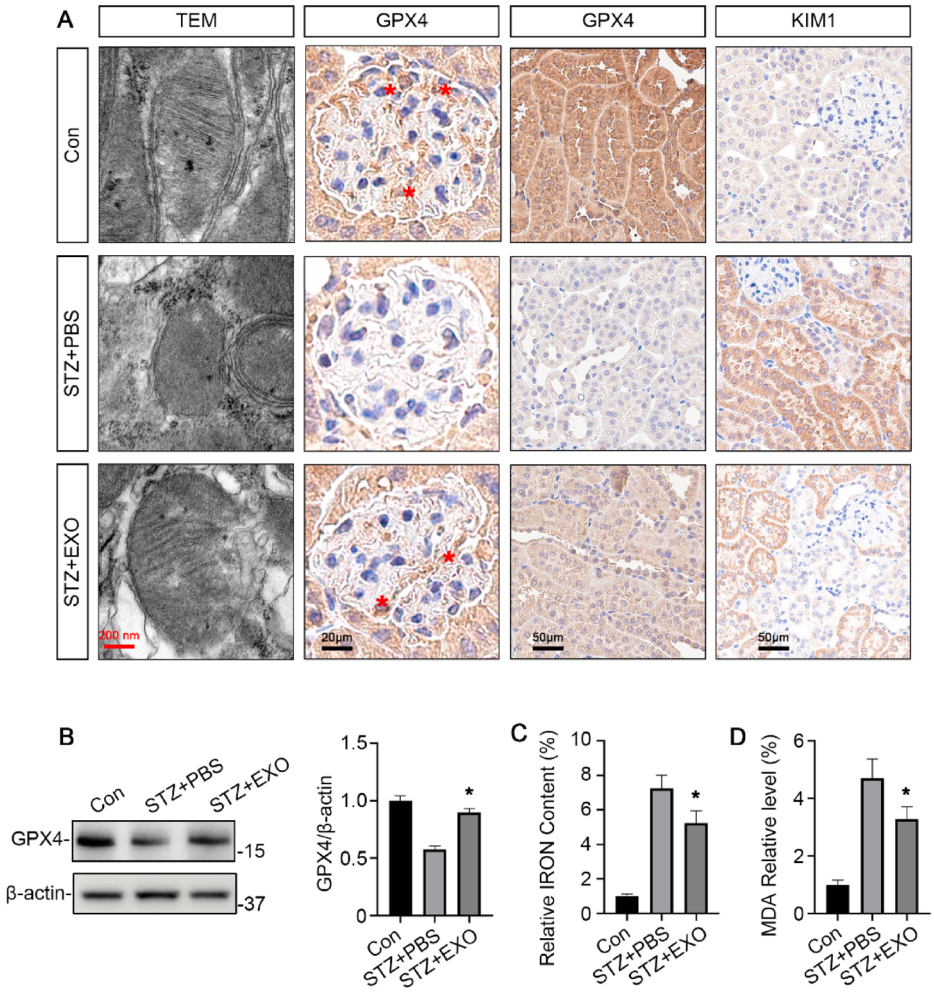


**Fig. 5**. BMSC-EXOs therapy suppresses ferroptosis and repairs mitochondrial and tubular damage in STZ-Induced diabetic kidney injury. (**A**) TEM images showing mitochondrial morphology in renal tissues. Immunohistochemical staining for GPX4 in the glomerular and tubular regions of the kidney. Red asterisks in (**A**) indicate positive GPX4 expression in the glomeruli. And immunohistochemical staining for KIM1 in different groups. (**B**) Western blot analysis of GPX4 expression in kidney tissues, with quantification normalized to β-actin. (**C**) Quantification of relative iron content and (**D**) MDA levels in renal tissues. Each bar represents the mean ± SD of the data derived from five independent experiments (n = 5). $^{*}p < 0.05$ versus STZ + PBS group. *GPX4* glutathione peroxidase 4, *KIM1* kidney injury molecule 1, *MDA* malondialdehyde, *TEM* transmission electron microscopy.

BMSC-EXOs treatment, further supporting the role of exsomes in repairing ferroptosis-associated tubular damage. GPX4 expression was quantified by immunoblot analysis (Fig. 5B). Moreover, ferroptosis markers, including iron content and MDA levels, were significantly elevated in the STZ + PBS group (Fig. 5C,D). BMSC-EXOs treatment significantly reduced these markers, indicating a reduction in ferroptosis-induced oxidative stress. These findings indicate that BMSC-EXOs not only inhibit ferroptosis but also repair mitochondrial and tubular integrity, thereby mitigating STZ-induced diabetic kidney injury.

## BMSC-EXOs repairs high glucose-induced podocyte injury by suppressing ferroptosis and apoptosis

BMSC-EXOs exerted significant reparative effects on HG-induced podocyte injury by restoring cell morphology, reducing stress marker expression, and suppressing both apoptosis and ferroptosis. Quantitative analysis of podocyte viability demonstrated a significant improvement following BMSC-EXOs treatment compared to the HG + PBS group (Fig. 6A). Western blot analysis revealed decreased expression of SYNPO and GPX4, along with elevated levels of early growth response protein 1 (EGR1), a stress-related marker, and cleaved caspase-3 in the HG + PBS group[36]. Notably, treatment with BMSC-EXOs restored SYNPO and GPX4 expression while reducing EGR1 and cleaved caspase-3 levels, indicating inhibition of ferroptosis and apoptosis (Fig. 6B,C). Bright-field imaging showed that podocytes under HG conditions (HG + PBS) exhibited pronounced morphological damage, including cell shrinkage and detachment (Fig. 6D). These structural abnormalities were alleviated by BMSC-EXOs treatment (HG + EXO), restoring podocyte morphology to a state more closely resembling that of the

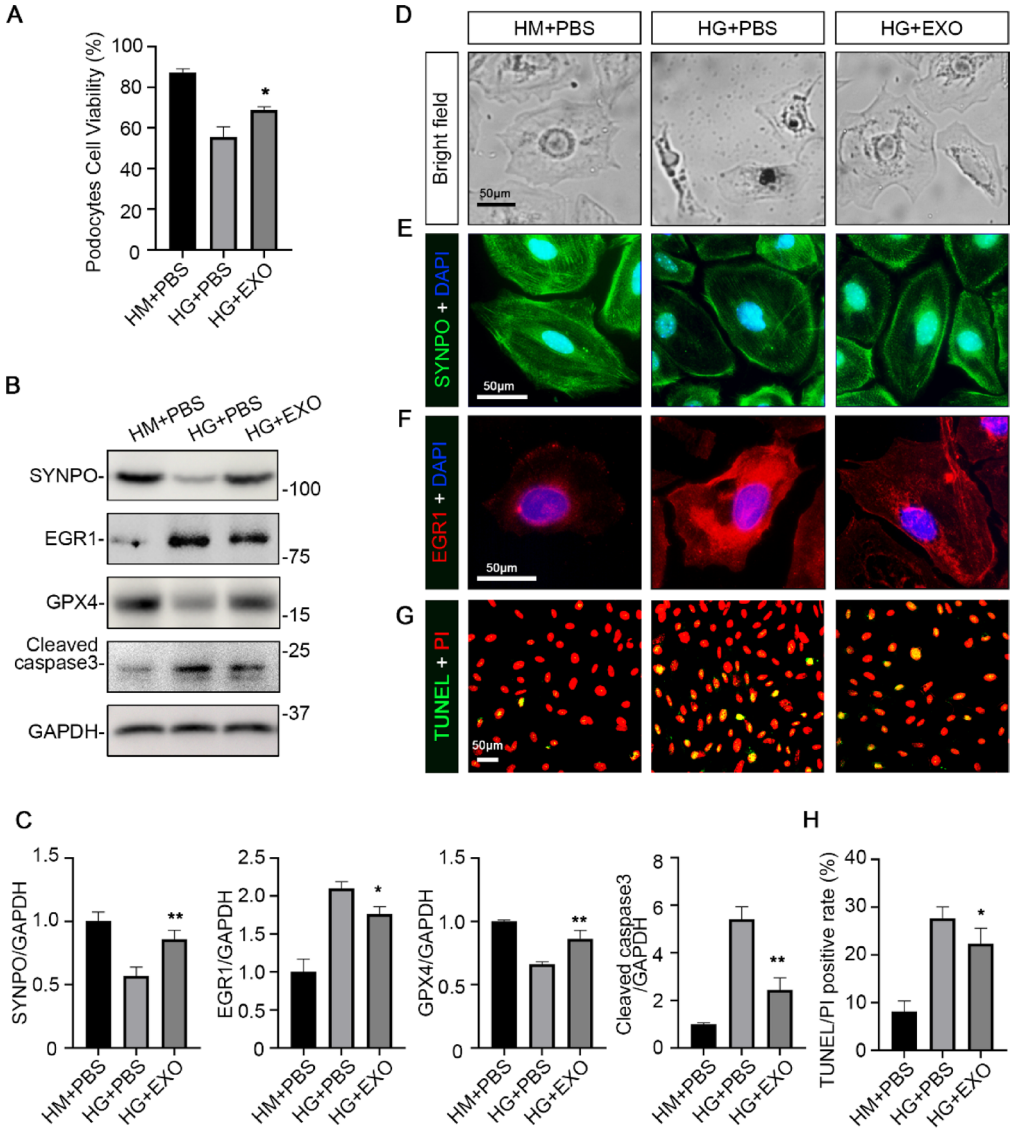


**Fig. 6**. BMSC-EXOs repairs high glucose-induced Podocyte injury by suppressing Ferroptosis and Apoptosis. (**A**) Quantification of podocytes cell viability in podocytes under normal glucose (HM + PBS), high glucose (HG + PBS), and high glucose with exosome treatment (HG + EXO). (**B**) Western blot analysis of SYNPO, EGR1, GPX4, cleaved caspase-3, and GAPDH expression in different groups of podocytes (**C**) and densitometric analysis of the blots. GAPDH served as a loading control. (**D**) Bright-field images showing morphological changes. (**E**) Immunofluorescence staining for SYNPO (green) and nuclear staining (DAPI, blue) in podocytes under different conditions. (**F**) Immunofluorescence staining for EGR1 (red) and nuclear staining (DAPI, blue) in podocytes. (**G**) TUNEL (green) and propidium iodide staining (PI, red) to assess apoptosis in podocytes. (**H**) The corresponding graph shows the percentage of TUNEL positive cells. Scale bar: 50 μm. Each bar represents the mean ± SD of the data derived from three independent experiments (n = 3). $^{*}p < 0.05$; $^{**}p < 0.01$ versus HG + PBS group. *DAPI* 4′,6-diamidino-2-phenylindole, *EGR1* early growth response protein 1, *GAPDH* glyceraldehyde-3-phosphate dehydrogenase, *GPX4* glutathione peroxidase 4, *TUNEL* terminal deoxynucleotidyl transferase dUTP nick end labelling, *SYNPO* synaptopodin.

control condition (HM + PBS). Immunofluorescence staining further revealed a marked reduction in SYNPO expression (green, Fig. 6E) and an increase in EGR1 expression (red, Fig. 6F) in the HG + PBS group. These alterations were reversed following BMSC-EXOs treatment, supporting structural restoration and decreased cellular stress. Apoptotic cell death, assessed by TUNEL and propidium iodide (PI) staining, was significantly elevated in the HG + PBS group but was markedly reduced following BMSC-EXOs treatment (Fig. 6G,H). Collectively, these findings demonstrate that BMSC-EXOs protect podocytes from HG-induced injury by preserving cellular integrity and mitigating both ferroptosis and apoptosis.

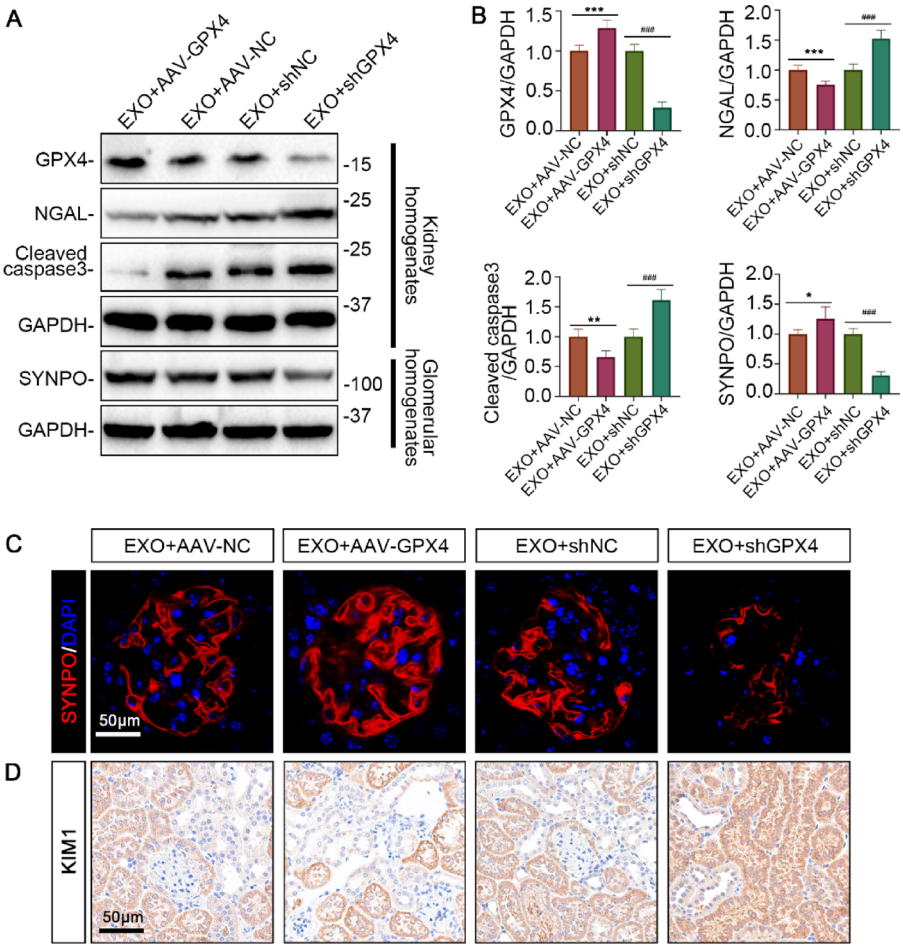


**Fig. 7**. BMSC-EXOs restore renal function in STZ-induced diabetic kidney injury via a GPX4-Dependent Mechanism. (**A**) Western blot analysis of renal GPX4, NGAL, and cleaved caspase3 expression in kidney homogenates, and SYNPO expression in glomerular homogenates. GAPDH served as a loading control. (**B**) Quantitative densitometry of the corresponding bands, normalized to GAPDH. (**C**) Immunofluorescence staining of SYNPO (red) in glomeruli and DAPI (blue) for nuclei. (**D**) Immunohistochemical staining of KIM1 in renal tubules. Each bar represents the mean ± SD of the data derived from five independent experiments ($n = 5$). $^{*}p < 0.05$; $^{**}p < 0.01$; $^{***}p < 0.001$ versus EXO + AAV-NC group. $^{\#\#\#}p < 0.001$ versus EXO + shNC group.

### BMSC-EXOs restore renal function in STZ-induced diabetic kidney injury via a GPX4-dependent mechanism

To investigate the functional role of GPX4 in BMSC-EXOs-mediated renoprotection, GPX4 overexpression was induced via transfection with an adeno-associated virus carrying the GPX4 gene (AAV-GPX4), while GPX4 knockdown was achieved using an AAV encoding a short hairpin RNA targeting GPX4 (AAV-shGPX4). Western blot analysis (Fig. 7A) revealed that renal GPX4 expression was markedly increased in the EXO + AAV-GPX4 group and significantly decreased in the EXO + AAV-shGPX4 group. Correspondingly, the expression levels of renal NGAL, and cleaved caspase-3 were significantly reduced in the EXO + AAV-GPX4 group but remained elevated in the EXO + AAV-shGPX4 group. Expression of SYNPO was restored following EXO treatment, further enhanced with GPX4 overexpression, and markedly decreased under GPX4-deficient conditions. These findings were further confirmed by densitometric quantification (Fig. 7B). Immunofluorescence (Fig. 7C) and immunohistochemistry (Fig. 7D) analyses supported these results. These results demonstrate that BMSC-EXOs restore renal function via GPX4-dependent inhibition of ferroptosis.

## Discussion

T1D is a chronic autoimmune disorder characterized by the progressive destruction of pancreatic islets and β-cells, leading to absolute insulin deficiency and severe metabolic dysfunction[2]. Although the precise mechanisms underlying β-cell injury remain incompletely understood, recent studies have identified ferroptosis as a critical contributor to β-cell dysfunction. This iron-dependent form of regulated cell death is primarily driven by dysregulation of iron metabolism, lipid peroxidation, and suppression of the antioxidant defense system. Notably, pancreatic β-cells possess inherently weak antioxidant capacity, rendering them highly susceptible to oxidative stress. Under hyperglycemic conditions, intracellular redox homeostasis is disrupted, promoting

lipid peroxidation and iron accumulation, which together trigger ferroptosis. Unlike apoptosis or necrosis, ferroptosis is characterized by the depletion of GPX4, a key antioxidant enzyme responsible for detoxifying lipid peroxides[37]. The loss of GPX4 further impairs the antioxidative capacity of β-cells, accelerating their destruction and perpetuating a vicious cycle of oxidative damage. This persistent ferroptosis-mediated injury not only impairs insulin secretion but also contributes to systemic diabetic complications, such as diabetic nephropathy[38]. Despite advancements in insulin replacement therapy, current treatment options for T1D remain insufficient in protecting and restoring β-cell function. Therefore, there is an urgent need to develop novel therapeutic strategies aimed at reducing hyperglycemia and ferroptosis, alleviating β-cell injury, and promoting the repair and regeneration of pancreatic islets.

MSC-EXOs have shown increasing therapeutic promise in T1D[13]. They exert immunomodulatory effects by modulating T cell-mediated inflammatory responses and contribute to the stabilization of body weight and blood glucose levels in T1D mouse models[9,39,40]. In T1D rat models, MSC-EXOs reduce blood glucose by increasing islet number, enhancing β-cell mass, and promoting insulin production[18,41]. Moreover, BMSC-EXOs protect against apoptosis in transplanted islet cells[42], and exosomal miR-29b-3p has been shown to enhance insulin sensitivity and regulate aging-associated insulin resistance[15]. The current study demonstrates that BMSC-EXOs effectively restore β-cell function, inhibit ferroptosis, and reduce lipid peroxidation, thereby preserving pancreatic islet integrity. Regarding body weight, BMSC-EXOs may indirectly mitigate diabetes-associated weight loss by stabilizing blood glucose levels, alleviating systemic inflammation, restoring energy metabolism, and enhancing mitochondrial activity. Furthermore, our findings reveal that these protective effects are mechanistically associated with increased GPX4 expression and reduced ferroptosis markers, including intracellular iron accumulation and MDA levels.

Diabetic nephropathy (DN) is a major microvascular complication of diabetes mellitus and the leading cause of end-stage renal disease (ESRD) worldwide[5,6]. It is primarily characterized by persistent proteinuria and/or a progressive decline in glomerular filtration rate. BMSC-derived exosomes (BMSC-EXOs), which contain various miRNAs, cytokines, and growth factors, have demonstrated significant efficacy in preserving the function of podocytes and endothelial cells, thereby exerting a preventative effect on DN progression. BMSC-EXOs have been shown to downregulate intercellular adhesion molecule 1 (ICAM-1), thereby inhibiting abnormal immune cell infiltration and reducing proinflammatory cytokine production[43]. Additionally, BMSC-EXOs promote autophagy by inhibiting the mTOR pathway, suppressing transforming growth factor-β (TGF-β) expression, and mitigating renal fibrosis[44]. Beyond their protective role in β-cell preservation, BMSC-EXOs also alleviate diabetic kidney injury by restoring podocyte integrity, reducing kidney injury markers, such as NGAL and KIM1, and improving renal function, as demonstrated in this study. Restoration of podocyte structure was associated with increased expression of SYNPO, a podocyte-specific marker frequently disrupted by hyperglycemia-induced inflammation and ROS. Components of exosomes have also been reported to attenuate activation of the Nucleotide-binding oligomerization domain (NOD)-like receptor family pyrin domain-containing 3 (NLRP3) inflammasome and reduce glomerular basement membrane thickening, thereby preserving podocyte architecture[45,46].

Although increasing evidence supports the role of exosomes in modulating cell death pathways, current studies on their regulation of ferroptosis remain limited, particularly in the context of diabetes and its complications. This study demonstrates that BMSC-EXOs effectively restore β-cell function, and inhibit ferroptosis, thereby preserving pancreatic islet integrity. In an STZ-induced diabetic mouse model, BMSC-EXOs therapy enhanced insulin production, stabilized blood glucose levels, and prevented diabetes-associated weight loss. These protective effects were mechanistically linked to increased GPX4 expression and reduced ferroptosis markers, including Iron overload and MDA levels. Beyond β-cell protection, BMSC-EXOs also alleviated diabetic kidney injury by restoring podocyte integrity, reducing kidney injury markers such as NGAL and KIM-1, and improving renal function. Exosome treatment mitigated renal ferroptosis by increasing GPX4 expression, reducing iron overload, and repairing mitochondrial damage. These findings suggest that BMSC-EXOs exert dual reparative effects by protecting both pancreatic β-cells and renal tissues in the diabetic setting.

To strengthen the causal relationship, mouse models with GPX4 overexpression and knockdown were established. The results showed that GPX4 overexpression significantly enhanced the protective effect of BMSC-EXOs, while GPX4 deficiency nearly abolished their therapeutic efficacy, directly validating the essential role of GPX4 in this mechanism. Evidence from other models also highlights the role of exosomal cargo in ferroptosis regulation. Adipose derived stem cells (ADSC)-derived exosomal miR-125b-5p attenuates inflammation-induced ferroptosis in pulmonary microvascular endothelial cells during sepsis-induced acute lung injury by modulating Keap1/Nrf2/GPX4 signalling, thereby improving sepsis-associated lung injury[47]. Cancer-associated fibroblast (CAF)-derived exosomal miR-188-3p in the regulation of ferroptosis in cervical cancer, with a particular focus on its targeting of GPX4[48]. Exosomes derived from human mesenchymal stem cells (hMSCs) reduce granulosa cell ferroptosis in chemotherapy-induced premature ovarian failure via the miR-26a-5p/PTEN/GPX4 axis[49]. In colorectal cancer (CRC) cells (SW480 and HCT116), adipocyte-derived exosomal microsomal triglyceride transfer protein (MTTP) was found to reverse ferroptosis in association with increased GPX4 and xCT expression[50]. Adipose tissue macrophage-derived exosomes (ATM-Exos) rich in miR-140-5p promote ferroptosis in cardiomyocytes by inhibiting Glutathione (GSH) synthesis through targeting solute carrier family 7 member 11 (SLC7A11)[51].

Future studies should explore the integrated regulatory effects of exosome cargo on the ferroptosis pathway. Despite these promising results, this study had certain limitations. The STZ-induced diabetes model replicates β-cell destruction but does not fully recapitulate the autoimmune pathogenesis of human T1D. Future studies should validate the therapeutic efficacy of BMSC-EXOs in autoimmune diabetes models and investigate additional mechanisms, such as Nrf2 activation. Systemic administration of EXOs primarily results in distribution to the

liver, spleen, and lungs, with limited accumulation in the kidney[52], leading to subtherapeutic concentrations at the target site.

## Conclusion

In conclusion, this study systematically revealed the therapeutic potential of BMSC-EXOs in T1D and its concomitant diabetic nephropathy and clarified their key role in β-cell and kidney protection through the GPX4-mediated ferroptosis inhibition mechanism. These findings provide a strong rationale for further exploration of exosome-based interventions for diabetes and its associated complications.

## Data availability

The datasets used and/or analyzed during the current study are available from the corresponding author Sijie Zhou on reasonable request via e-mail [fcczhousj@zzu.edu.cn] (mailto:fcczhousj@zzu.edu.cn).

Received: 10 February 2025; Accepted: 17 October 2025
Published online: 19 November 2025

## References

1. Saeedi, P. et al. Global and regional diabetes prevalence estimates for 2019 and projections for 2030 and 2045: Results from the International Diabetes Federation Diabetes Atlas, 9(th) edition. *Diabetes Res. Clin. Pract.* **157**, 107843. https://doi.org/10.1016/j.diabres.2019.107843 (2019).
2. Quinn, L. M., Thrower, S. L. & Narendran, P. What is type 1 diabetes?. *Medicine* **50**, 619–624. https://doi.org/10.1016/j.mpmed.2022.07.002 (2022).
3. DeWitt, D. E. & Hirsch, I. B. Outpatient insulin therapy in type 1 and type 2 diabetes mellitusscientific review. *JAMA* **289**, 2254–2264. https://doi.org/10.1001/jama.289.17.2254 (2003).
4. Addissouky, T. A., Ali, M. M. A., El Sayed, I. E. T. & Wang, Y. Type 1 diabetes mellitus: Retrospect and prospect. *Bull. Natl. Res. Cent.* **48**, 42. https://doi.org/10.1186/s42269-024-01197-z (2024).
5. Ritz, E., Rychlík, I., Locatelli, F. & Halimi, S. End-stage renal failure in type 2 diabetes: A medical catastrophe of worldwide dimensions. *Am. J. Kidney Dis.* **34**, 795–808. https://doi.org/10.1016/S0272-6386(99)70035-1 (1999).
6. Sulaiman, M. K. Diabetic nephropathy: Recent advances in pathophysiology and challenges in dietary management. *Diabetol. Metab. Syndr.* **11**, 7. https://doi.org/10.1186/s13098-019-0403-4 (2019).
7. Pittenger, M. F. et al. Mesenchymal stem cell perspective: cell biology to clinical progress. *NPJ Regen. Med.* **4**, 22. https://doi.org/10.1038/s41536-019-0083-6 (2019).
8. Wu, X. et al. Mesenchymal stromal cell therapies: Immunomodulatory properties and clinical progress. *Stem Cell Res. Ther.* **11**, 345. https://doi.org/10.1186/s13287-020-01855-9 (2020).
9. Shigemoto-Kuroda, T. et al. MSC-derived extracellular vesicles attenuate immune responses in two autoimmune murine models: Type 1 diabetes and uveoretinitis. *Stem Cell Rep.* **8**, 1214–1225. https://doi.org/10.1016/j.stemcr.2017.04.008 (2017).
10. Abdulmalek, O. A. A. Y. et al. Therapeutic applications of stem cell-derived exosomes. *Int. J. Mol. Sci.* **25**, 3562 (2024).
11. Zhuang, W. Z. et al. Mesenchymal stem/stromal cell-based therapy: Mechanism, systemic safety and biodistribution for precision clinical applications. *J. Biomed. Sci.* **28**, 28. https://doi.org/10.1186/s12929-021-00725-7 (2021).
12. Di Bella, M. A. Overview and update on extracellular vesicles: Considerations on exosomes and their application in modern medicine. *Biology (Basel)* **11**, 804. https://doi.org/10.3390/biology11060804 (2022).
13. Jiao, Y. R. et al. Exosomes derived from mesenchymal stem cells in diabetes and diabetic complications. *Cell Death Dis.* **15**, 271. https://doi.org/10.1038/s41419-024-06659-w (2024).
14. Zhang, Z. G., Buller, B. & Chopp, M. Exosomes—Beyond stem cells for restorative therapy in stroke and neurological injury. *Nat. Rev. Neurol.* **15**, 193–203. https://doi.org/10.1038/s41582-018-0126-4 (2019).
15. Su, T. et al. Bone marrow mesenchymal stem cells-derived exosomal MiR-29b-3p regulates aging-associated insulin resistance. *ACS Nano* **13**, 2450–2462. https://doi.org/10.1021/acsnano.8b09375 (2019).
16. Asgarpour, K. et al. Exosomal microRNAs derived from mesenchymal stem cells: Cell-to-cell messages. *Cell Commun. Signal.* **18**, 149. https://doi.org/10.1186/s12964-020-00650-6 (2020).
17. Yuan, Y. G. et al. Biogenesis, composition and potential therapeutic applications of mesenchymal stem cells derived exosomes in various diseases. *Int. J. Nanomed.* **18**, 3177–3210. https://doi.org/10.2147/ijn.S407029 (2023).
18. Sabry, D., Marzouk, S., Zakaria, R., Ibrahim, H. A. & Samir, M. The effect of exosomes derived from mesenchymal stem cells in the treatment of induced type 1 diabetes mellitus in rats. *Biotechnol. Lett.* **42**, 1597–1610. https://doi.org/10.1007/s10529-020-02908-y (2020).
19. Wang, H. et al. Emerging role of ferroptosis in diabetic kidney disease: Molecular mechanisms and therapeutic opportunities. *Int. J. Biol. Sci.* **19**, 2678–2694. https://doi.org/10.7150/ijbs.81892 (2023).
20. Li, J., Zheng, S., Fan, Y. & Tan, K. Emerging significance and therapeutic targets of ferroptosis: A potential avenue for human kidney diseases. *Cell Death Dis.* **14**, 628. https://doi.org/10.1038/s41419-023-06144-w (2023).
21. Jin, E. J. et al. Ferroptosis and iron metabolism in diabetes: Pathogenesis, associated complications, and therapeutic implications. *Front. Endocrinol. (Lausanne)* **15**, 1447148. https://doi.org/10.3389/fendo.2024.1447148 (2024).
22. Wang, M., Mo, D., Zhang, N. & Yu, H. Ferroptosis in diabetic cardiomyopathy: Advances in cardiac fibroblast-cardiomyocyte interactions. *Heliyon* **10**, e35219. https://doi.org/10.1016/j.heliyon.2024.e35219 (2024).
23. Ru, Q. et al. Iron homeostasis and ferroptosis in human diseases: Mechanisms and therapeutic prospects. *Signal Transduct. Target. Ther.* **9**, 271. https://doi.org/10.1038/s41392-024-01969-z (2024).
24. Kowluru, A. Oxidative stress in cytokine-induced dysfunction of the pancreatic beta cell: Known knowns and known unknowns. *Metabolites* **10**, 480. https://doi.org/10.3390/metabo10120480 (2020).
25. Chen, J., Stimpson, S. E., Fernandez-Bueno, G. A. & Mathews, C. E. Mitochondrial reactive oxygen species and type 1 diabetes. *Antioxid. Redox Signal.* **29**, 1361–1372. https://doi.org/10.1089/ars.2017.7346 (2018).
26. Zheng, Y., Sun, J., Luo, Z., Li, Y. & Huang, Y. Emerging mechanisms of lipid peroxidation in regulated cell death and its physiological implications. *Cell Death Dis.* **15**, 859. https://doi.org/10.1038/s41419-024-07244-x (2024).
27. Wang, X. et al. Ferroptosis is essential for diabetic cardiomyopathy and is prevented by sulforaphane via AMPK/NRF2 pathways. *Acta Pharm. Sin. B* **12**, 708–722. https://doi.org/10.1016/j.apsb.2021.10.005 (2022).
28. Pei, Z. et al. FUNDC1 insufficiency sensitizes high fat diet intake-induced cardiac remodeling and contractile anomaly through ACSL4-mediated ferroptosis. *Metabolism* **122**, 154840. https://doi.org/10.1016/j.metabol.2021.154840 (2021).
29. Wang, H. et al. VDR activation attenuates renal tubular epithelial cell ferroptosis by regulating Nrf2/HO-1 signaling pathway in diabetic nephropathy. *Adv. Sci. (Weinh.)* **11**, e2305563. https://doi.org/10.1002/advs.202305563 (2024).
30. Rai, A. et al. A protocol for isolation, purification, characterization, and functional dissection of exosomes. *Methods Mol. Biol.* **2261**, 105–149. https://doi.org/10.1007/978-1-0716-1186-9_9 (2021).

31. García-Ocaña, A. et al. Transgenic overexpression of hepatocyte growth factor in the beta-cell markedly improves islet function and islet transplant outcomes in mice. *Diabetes* **50**, 2752–2762. https://doi.org/10.2337/diabetes.50.12.2752 (2001).
32. Zhou, S. et al. Genetic and pharmacologic targeting of glycogen synthase kinase 3β reinforces the Nrf2 antioxidant defense against podocytopathy. *J. Am. Soc. Nephrol.* **27**, 2289–2308. https://doi.org/10.1681/asn.2015050565 (2016).
33. Zhang, J. et al. Microdose lithium protects against pancreatic islet destruction and renal impairment in streptozotocin-elicited diabetes. *Antioxidants (Basel)* **10**, 138. https://doi.org/10.3390/antiox10010138 (2021).
34. Crowe, A. R. & Yue, W. Semi-quantitative determination of protein expression using immunohistochemistry staining and analysis: An integrated protocol. *Bio Protoc.* **9**, e3465 (2019).
35. Jörns, A. et al. Immune cell infiltration, cytokine expression, and beta-cell apoptosis during the development of type 1 diabetes in the spontaneously diabetic LEW.1AR1/Ztm-iddm rat. *Diabetes* **54**, 2041–2052. https://doi.org/10.2337/diabetes.54.7.2041 (2005).
36. Yin, L., Zhang, J. & Sun, Y. Early growth response-1 is a new substrate of the GSK3β-FBXW7 axis. *Neoplasia* **34**, 100839. https://doi.org/10.1016/j.neo.2022.100839 (2022).
37. Li, S., Zheng, L., Zhang, J., Liu, X. & Wu, Z. Inhibition of ferroptosis by up-regulating Nrf2 delayed the progression of diabetic nephropathy. *Free Radic. Biol. Med.* **162**, 435–449. https://doi.org/10.1016/j.freeradbiomed.2020.10.323 (2021).
38. Xie, L., Fang, B. & Zhang, C. The role of ferroptosis in metabolic diseases. *Biochim. Biophys. Acta (BBA) Mol. Cell Res.* **1870**, 119480. https://doi.org/10.1016/j.bbamcr.2023.119480 (2023).
39. Nojehdehi, S. et al. Immunomodulatory effects of mesenchymal stem cell-derived exosomes on experimental type-1 autoimmune diabetes. *J. Cell Biochem.* **119**, 9433–9443. https://doi.org/10.1002/jcb.27260 (2018).
40. Rahman, M. J., Regn, D., Bashratyan, R. & Dai, Y. D. Exosomes released by islet-derived mesenchymal stem cells trigger autoimmune responses in NOD mice. *Diabetes* **63**, 1008–1020. https://doi.org/10.2337/db13-0859 (2014).
41. Mahdipour, E., Salmasi, Z. & Sabeti, N. Potential of stem cell-derived exosomes to regenerate β islets through Pdx-1 dependent mechanism in a rat model of type 1 diabetes. *J. Cell. Physiol.* **234**, 20310–20321. https://doi.org/10.1002/jcp.28631 (2019).
42. Wen, D., Peng, Y., Liu, D., Weizmann, Y. & Mahato, R. I. Mesenchymal stem cell and derived exosome as small RNA carrier and Immunomodulator to improve islet transplantation. *J. Control. Release* **238**, 166–175. https://doi.org/10.1016/j.jconrel.2016.07.044 (2016).
43. Nagaishi, K. et al. Mesenchymal stem cell therapy ameliorates diabetic nephropathy via the paracrine effect of renal trophic factors including exosomes. *Sci. Rep.* **6**, 34842. https://doi.org/10.1038/srep34842 (2016).
44. Ebrahim, N. et al. Mesenchymal stem cell-derived exosomes ameliorated diabetic nephropathy by autophagy induction through the mTOR signaling pathway. *Cells* **7**, 226. https://doi.org/10.3390/cells7120226 (2018).
45. Huang, D. et al. Exosome biogenesis and lysosome function determine podocyte exosome release and glomerular inflammatory response during hyperhomocysteinemia. *Am. J. Pathol.* **192**, 43–55. https://doi.org/10.1016/j.ajpath.2021.10.005 (2022).
46. Li, Z. et al. Exosomes regulate NLRP3 inflammasome in diseases. *Front. Cell Dev. Biol.* **9**, 802509. https://doi.org/10.3389/fcell.2021.802509 (2022).
47. Shen, K. et al. miR-125b-5p in adipose derived stem cells exosome alleviates pulmonary microvascular endothelial cells ferroptosis via Keap1/Nrf2/GPX4 in sepsis lung injury. *Redox Biol.* **62**, 102655. https://doi.org/10.1016/j.redox.2023.102655 (2023).
48. Li, X. & Han, M. Exosomal miRNA-188-3p derived from cancer-associated fibroblasts promotes ferroptosis in cervical cancer: Medical biothermal image analysis. *SLAS Technol.* **33**, 100313. https://doi.org/10.1016/j.slast.2025.100313 (2025).
49. Chen, J. et al. Exosomes derived from human mesenchymal stem cells mitigate follicular interstitial cell ferroptosis via the miR-26a-5p/PTEN/GPX4 axis in rats with chemotherapy-induced premature ovarian insufficiency. *Int. J. Nanomed.* **20**, 10195–10212. https://doi.org/10.2147/ijn.S532207 (2025).
50. Zhang, Q. et al. Adipocyte-derived exosomal MTTP suppresses ferroptosis and promotes chemoresistance in colorectal cancer. *Adv. Sci.* **9**, 2203357. https://doi.org/10.1002/advs.202203357 (2022).
51. Zhao, X. et al. Adipose tissue macrophage-derived exosomes induce ferroptosis via glutathione synthesis inhibition by targeting SLC7A11 in obesity-induced cardiac injury. *Free Radic. Biol. Med.* **182**, 232–245. https://doi.org/10.1016/j.freeradbiomed.2022.02.033 (2022).
52. Lázaro-Ibáñez, E. et al. Selection of fluorescent, bioluminescent, and radioactive tracers to accurately reflect extracellular vesicle biodistribution in vivo. *ACS Nano* **15**, 3212–3227. https://doi.org/10.1021/acsnano.0c09873 (2021).


## Acknowledgements

This work was supported by the National Natural Science Foundation of China (U21A20348), Scientific and Technological Innovation Young Top Talents in Central Plains, Tianjian Laboratory of Advanced Biomedical Sciences Project. The funders had no role in the study design, data collection, interpretation, or manuscript preparation and approval.

## Author contributions

S.Z. designed the research; J.Z. and L.W. conducted the experiments; J.Z. and D.L. analyzed the data; J.Z., S.Z., Z.L. (Zhi. Liu.) and Z.L. (Zhang. Liu.) contributed to the discussion; J.Z., and S.Z. wrote the manuscript; all authors reviewed and approved the final version of the paper.

## Funding

This work was supported the National Natural Science Foundation of China (U21A20348), Scientific and Technological Innovation Young Top Talents in Central Plains, Tianjian Laboratory of Advanced Biomedical Sciences Project.

## Declarations

## Competing interests

The authors declare no competing interests.

## Institutional review board statement

The animal study protocol was approved by the Ethics Committee of Zhengzhou University (ZZU-LAC20230804[20]).

## Additional information

**Supplementary Information** The online version contains supplementary material available at https://doi.org/1

0.1038/s41598-025-25204-z.

**Correspondence** and requests for materials should be addressed to Z.L., Z.L. or S.Z.